RSC Advances

Cite this: *RSC Advances*, 2012, **2**, 4364–4369

www.rsc.org/advances

PAPER

Hybrid structure of zinc oxide nanorods and three dimensional graphene foam for supercapacitor and electrochemical sensor applications

Xiaochen Dong,*[a] Yunfa Cao,[a] Jing Wang,[b] Mary B. Chan-Park,[b] Lianhui Wang,[a] Wei Huang[a] and Peng Chen*[b]

Received 14th December 2011, Accepted 28th February 2012
DOI: 10.1039/c2ra01295b

A hybrid structure of zinc oxide (ZnO) on three dimensional (3D) graphene foam has been synthesized by chemical vapor deposition (CVD) growth of graphene followed by a facial *in situ* precipitation of ZnO nanorods under hydrothermal conditions. Scanning electron microscopy (SEM) and X-ray diffraction (XRD) are used to characterize the morphology and structure of graphene/ZnO hybrids. The results show that the ZnO nanorods have high crystallinity and cluster uniformly on graphene skeleton to form flower-like nanostructures. Serving as a free-standing electrode, the electrochemical and biosensing performance of graphene/ZnO hybrids are studied by cyclic voltammetry, electrochemical impedance spectroscopy, galvanostatic charge–discharge and amperometric measurements. It is found that the graphene/ZnO hybrids display superior capacitive performance with high specific capacitance ($\sim$400 F g^{-1}) as well as excellent cycle life, making them suitable for high-performance energy storage applications. Furthermore, the graphene/ZnO hybrids exhibit high sensitivity for detection of $[Fe(CN)_6]^{3+}$ and dopamine, with the extrapolated lower detection limits of $\sim$1.0 μM and $\sim$10.0 nM respectively. These results demonstrate the potential of free-standing graphene/ZnO hybrid electrodes for the development of highly sensitive electrochemical sensors.

1. Introduction

Graphene, a monolayer of carbon atoms hexagonally bonded into a two dimensional sheet,[1,2] has recently been explored for the applications in energy storage[3,4] and biosensors[5–9] due to its chemical stability, extraordinarily high electrical conductivity, large specific surface area, and great mechanical strength.[10,11] In most applications, particularly when a small quantity of graphene is not sufficient, graphene is prepared through chemical or thermal reduction of graphene oxide exfoliated from graphite.[12,13] The resulting graphene films or composites, however, exhibit severely compromised conductivity due to the abundant existence of defects and oxygen-containing chemical groups, and numerous non-ideal contacts between graphene sheets. In addition, the strong π–π interaction between graphene sheets leads to severe aggregation and decrease of its specific surface area.[14] Both of these shortcomings seriously limit the performance of graphene based supercapacitors, sensors and other devices. The recently demonstrated three dimensional (3D) graphene foam synthesized by chemical vapor deposition (CVD) on nickel foam substrates[15] overcomes these problems. The CVD-grown 3D graphene can provide a highly conductive network due to the high intrinsic conductivity of defect-free graphene and absence of inter-sheet junction-resistance in this seamlessly continuous network. In addition, the porous nature of this new graphene material offers large specific surface area (up to $\sim$850 m^{2}g^{-1})[15] and is suitable to make functional composites by filling the pores with nanoparticles, polymers or other functional materials.[16]

Transition metal oxides, such as MnO_2,[17] Co_3O_4,[18] ZnO,[19] NiO[20] and MoO_3,[21] have been widely employed for electrochemical capacitors with high power density, taking advantage of their fast redox kinetics. But, the poor conductivity, low mechanical and chemical stability of these materials usually demand the addition of conductive phase (*e.g.*, carbon black) to enhance its charge transfer rate and supporting matrix/substrate. Various approaches have been explored to integrate carbonaceous materials and transition metal oxides.[22,23] In addition, utilizing their electrochemical active properties and molecular sizes, metal oxide nanostructures have been used for various electrochemical sensors.[24,25] In particular, ZnO nanostructures are promising materials in optics, optoelectronics, sensors, supercapacitors, and actuators due to their semiconducting, piezoelectronic, and pyroelectric properties.[26,27] Nanostructured ZnO possesses high specific surface area, biocompatibility and excellent electrochemical activity, making it desirable for high performance supercapacitors and biosensors.[28]

[a]*Key Laboratory for Organic Electronics & Information Displays (KLOEID), Institute of Advanced Materials (IAM), Nanjing University of Posts and Telecommunications (NUPT), 9 Wenyuan Road, Nanjing, 210046, China. E-mail: iamxcdong@njupt.edu.cn; Tel: 86-25-85866396*
[b]*School of Chemical and Biomedical Engineering, Nanyang Technological University, Singapore 637457. E-mail: chenpeng@ntu.edu.sg; Tel: 65-65141086*

In this work, we present a novel hybrid structure of ZnO and graphene, synthesized by chemical vapor deposition (CVD) growth of 3D graphene followed by a facial *in situ* precipitation process of ZnO nanorods under hydrothermal conditions. Furthermore, we demonstrate the use of graphene/ZnO as a free-standing monolithic electrode for supercapacitor and electrochemical sensor applications.

2. Results and discussion

Fig. 1a illustrates the synthetic process of graphene/ZnO hybrid structures, which is detailed in the Experimental section. The photograph of a graphene/ZnO hybrid shows that it can stand alone and is flexible (Fig. 1a). Fig. 1b shows the Raman spectra of 3D graphene, ZnO and the graphene/ZnO hybrid, respectively. The Raman spectrum of graphene foam contains two prominent peaks at ~1570 and 2700 cm^{-1}, corresponding to the characteristic G and 2D band of graphene.[29] The absence of a D band (~1350 cm^{-1}) indicates that the graphene foam is of high quality (*i.e.*, lack of defects).[30] The integral ratio of the 2D and G bands indicates that the as-grown graphene foam is mainly few-layered.[31] The Raman spectrum of ZnO contains a sharp peak at ~424 cm^{-1} corresponding to the vibration mode of E_2, and several smaller peaks at ~330, ~574 and ~1125 cm^{-1} resulting from the multiple-phono scattering process.[32] The spectrum of graphene/ZnO hybrid is essentially the superimposition of that of ZnO and graphene, except the appearance of a small D band (likely arising from the defects introduced in the hydrothermal condition[33]) and right shifts of G and 2D band (likely due to the doping effects of ZnO[34]).

The morphologies of graphene foam and graphene/ZnO are examined by SEM, as shown in Fig. 2. It can be seen from Fig. 2a and the previous report[15] that the 3D graphene foam is a porous structure (pore size ~30–100 μm) with a smooth surface, identical to that of the nickel foam resulting from the conformal

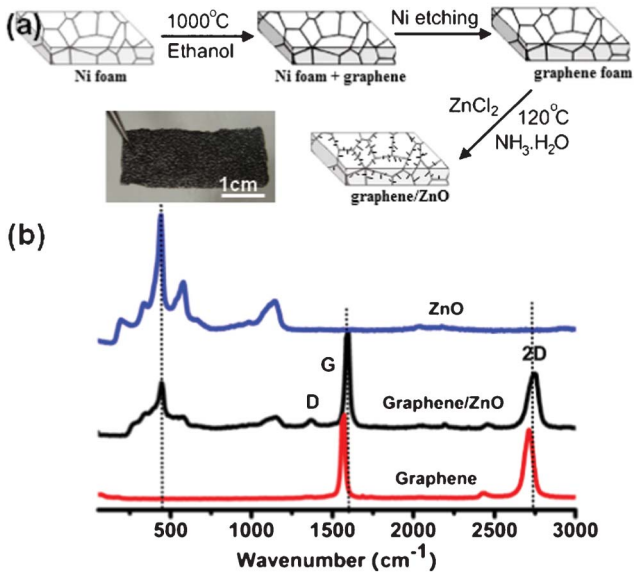

Fig. 1 (a) Schematic of the synthesis process and a photograph of graphene/ZnO hybrid. (b) Raman spectra of bare 3D graphene, ZnO and graphene/ZnO hybrid.

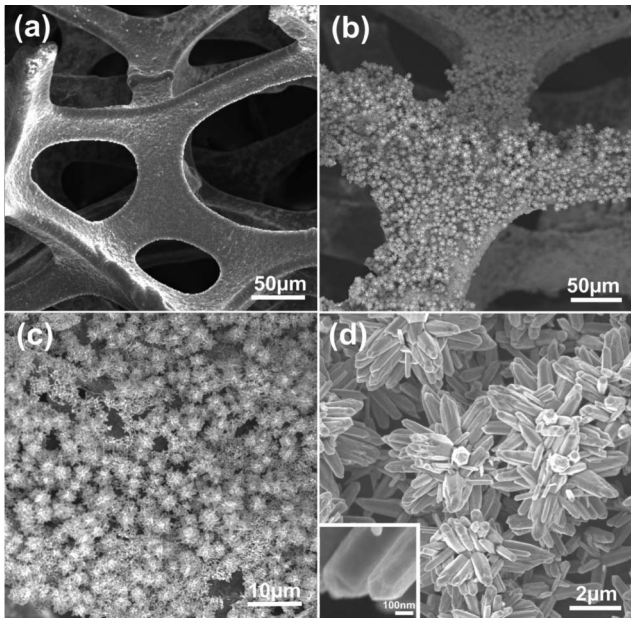

Fig. 2 SEM images of the samples. (a) SEM image of 3D graphene foam. (b–d) SEM images of graphene/ZnO hybrids with different magnifications. The inset of (d) shows the morphology of a single ZnO nanorod at a high magnification.

CVD growth. In the graphene/ZnO hybrid, nanostructured ZnO clusters are densely anchored onto the both sides of graphene surface (Fig. 2b). At higher magnification, it is observed that ZnO nanostructures are flower-like bundles of individual nanorods (Fig. 2c and d). The diameter of the ZnO nanorods is about 100–200 nm and the length is about 1.0 μm. They diverge in the cluster with the surface fully exposed, providing a large surface area for electrochemical activities. Brunauer–Emmett–Teller (BET) nitrogen adsorption–desorption characterization was conducted at 77 K, as shown in Fig. 3. The specific surface area of the hybrid is calculated to be 214.5 m^2 g^{-1}.

To further characterize the crystal structure of ZnO on the surface of 3D graphene, the X-ray diffraction (XRD) is

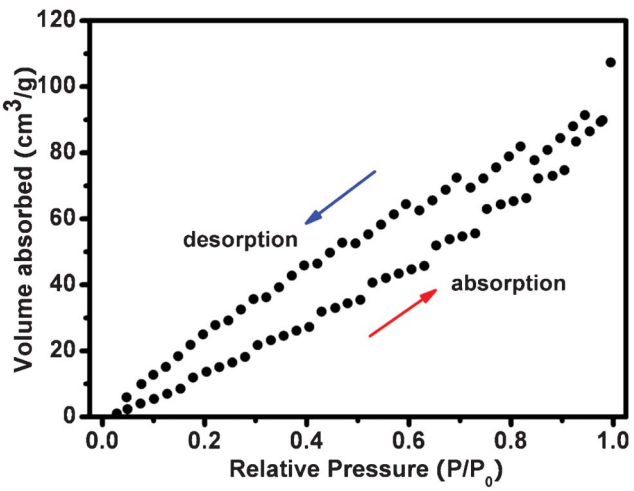

Fig. 3 N_2 adsorption–desorption isotherm of a 3D grapheme/ZnO hybrid.

performed (Fig. 4). In comparison, the XRD patterns of bare 3D graphene and ZnO are also shown. The 3D graphene shows two diffraction peaks at $2\theta = 26.5^\circ$ and 54.6°, which are attributed to the (002) and (004) reflections of graphitic carbon, respectively (JCPDS 75-1621). The sharp peak at 26.5° indicates high crystallinity and an interlayer space of ~0.34 nm of the defect-free CVD grown graphene, which is similar to the natural graphite but distinct to the commonly used defective reduced graphene oxide.[35] The diffraction peaks of ZnO appear at 2θ values of 31.9°, 34.5°, 36.4°, 47.6°, 56.6°, 62.9°, 66.5°, 68.1° and 69.2°. All these characteristic diffraction peaks can be indexed to the ZnO hexagonal Wurtzite structure of (100), (002), (101), (102), (110), (103), (200), (112) and (201) planes, which match well with the standard ZnO peaks (JCPDS 36-1451).[36] The XRD pattern of the graphene/ZnO hybrid is the perfect addition of that from bare graphene and ZnO, indicating that ZnO nanostructures on graphene have high crystallinity.

The graphene/ZnO hybrid can serve as a light free-standing working electrode for electrochemical measurements. Cyclic voltammetry (CV) curves (at a scan rate of 20 mV s^{-1}) of the free-standing graphene foam and graphene/ZnO hybrid electrodes in 2.0 M KOH electrolyte are presented in Fig. 5a. Clearly, the CV of the graphene/ZnO hybrid electrode shows a pair of Faradaic redox peaks (~0.31 V and 0.46 V). As demonstrated previously,[37,38] these redox peaks result from the intercalation and deintercalation of K^+ from the electrolyte into ZnO: $ZnO + K^+ + e^- \leftrightarrow ZnOK$. The highly conductive graphene foam facilitates the charge transfer and conduction from the reactions. In contrast, the CV of bare graphene foam is a narrow rectangle, indicating the absence of electrochemical activity and a small capacitance. These results also suggest that the large capacitance of graphene/ZnO originates from the pseudocapacitance of the electrochemically active ZnO nanorods instead of the double-layer capacitance from the graphene skeleton. Fig. 5b shows the CV curves of the graphene/ZnO hybrid electrode at different scan rates. With the increase of scan rate, the current response increases accordingly, with more prominent redox peaks. It indicates that the redox reaction of ZnO on graphene is rapid and reversible. To further evaluate the electrochemical capacitance of the graphene/ZnO

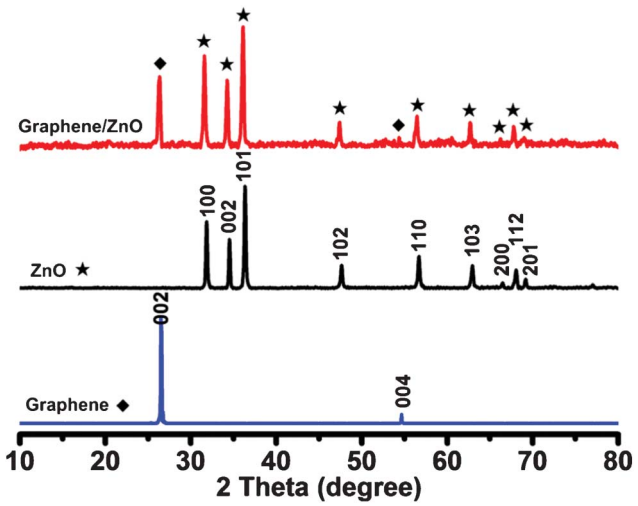

Fig. 4 Typical XRD patterns of 3D graphene, ZnO and graphene/ZnO hybrid.

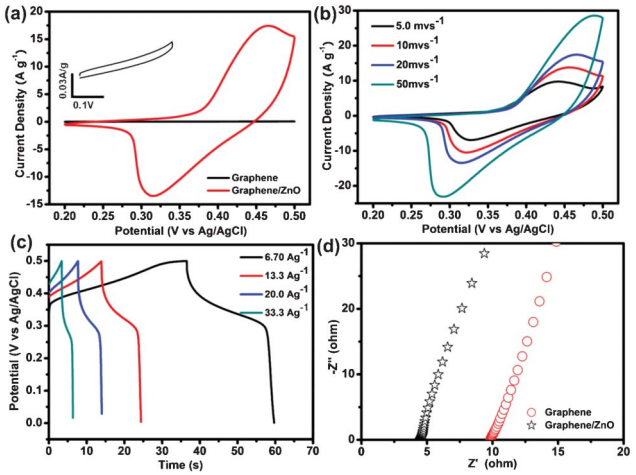

Fig. 5 (a) CV curves of free-standing graphene and graphene/ZnO hybrid electrodes at a scan rate of 20 mV s^{-1} in 2.0 M KOH electrolyte. The inset shows the enlarged CV curve of a graphene foam electrode. (b) CV curves of the graphene/ZnO hybrid electrode at different scan rates of 5 mV s^{-1}, 10 mV s^{-1}, 20 mV s^{-1}, and 50 mV s^{-1}. (c) Galvanostatic charge–discharge curves of the graphene/ZnO hybrid electrode at different current densities. (d) Nyquist plots of graphene foam and graphene/ZnO hybrid electrodes.

hybrid electrode, the galvanostatic charge–discharge curves are measured at a series of current densities within the potential range 0 to 0.5 V (Fig. 5c). The nonlinear shape of the discharge curves is expected from the pseudocapacitance behavior of metal oxides resulting from the electrochemical adsorption–desorption or redox reaction at the electrode and electrolyte interface, which is distinct from the linear triangular shape expected from a double-layer capacitor.[39,40] The average specific capacitance of the graphene/ZnO hybrid electrode can be calculated using the formula: $C_m = It/\Delta Vm$, where C_m, I, t and ΔV are the specific capacitance of electrodes (F g^{-1}), the charge–discharge current (A), the discharge time (s) and the mass of graphene/ZnO hybrid electrode, respectively.[41] A specific capacitance of 316, 263, 235.8 and 210.7 F g^{-1} can be delivered at the current density of 6.70, 13.3, 20.0, 33.3 Ag^{-1}, respectively. Note that the specific capacitance remains high even at high current densities. The value is much higher than that of the bare graphene foam (56 F g^{-1} at current density 6.0 A g^{-1}). It is also significantly higher than the previous demonstrated graphene/ZnO hybrid electrodes.[42,43]

The superior electrochemical performance of the graphene/ZnO hybrid electrode is further confirmed by the electrochemical impedance spectroscopy (EIS) measurements. Fig. 5d shows the Nyquist plots of the EIS spectra for the graphene and graphene/ZnO hybrid electrodes. The equivalent series resistance (ESR) (including the resistance of KOH aqueous solution, the intrinsic resistance of the electroactive material and the contact resistance at the interface between the electrode and current collector[44]) can be obtained from the x-intercept of the Nyquist plots. As shown in Fig. 5d, the ESR of the graphene/ZnO electrode (4.2 Ω) is much smaller than that of the bare graphene electrode (9.0 Ω). In the Nyquist plot, the slope at low frequencies can be used to evaluate the capacitive behavior of the electrode.[45] The nearly vertical slope of the graphene/ZnO suggests that it has nearly ideal capacitive behaviour.

Fig. 6a shows the cyclic performance of the graphene/ZnO hybrid electrodes examined by continuous galvanostatic charge–discharge measurements for 1000 cycles. At a current density of 6.70 A g^{-1}, the specific capacitance of graphene/ZnO hybrid electrode increases ~20% during the first 200 cycles and remains stable afterwards. It demonstrates the high stability and reversibility of the graphene/ZnO hybrid electrode. The initial increase of specific capacitance during the charge–discharge cycles can be attributed to the activation process to allow the trapped cations to gradually diffuse out.[46] The CV curves before and after 1000 charge–discharge cycles are nearly identical as shown in Fig. 6b. Our experiments (Fig. 5 and 6) demonstrate the potential of the free-standing graphene/ZnO electrode in supercapacitor applications. Its excellent performance can be attributed to: (1) electroactive property of ZnO; (2) large surface area provided the 3D nanostructures; (3) multiplexed highly-conductive pathways provided by the 3D graphene scaffold; (4) firm and stable integration between ZnO nanorods and graphene; (5) high mechanical robustness and chemical stability of graphene. These characteristics are also highly desirable for electrochemical sensing. Therefore, we sought to test the potential of a free-standing graphene/ZnO hybrid electrode for electrochemical sensors.

Ferricyanide $[Fe(CN)_6]^{3+}$ is a classic electroactive substance that is often employed as a mediator in various electrochemical sensors.[47] In these sensors, the electrochemical signal of ferricyanide is detected as the reporter of molecular binding events which block or increase the diffusion of ferricyanide onto the electrode. Thus, we first examined the ability of the graphene/ZnO electrode for detection of ferricyanide. Fig. 7a shows the CV curves of graphene/ZnO and glass carbon electrodes in 1.0 mM $K_3[Fe(CN)_6]$ in the range from −0.2 V to 0.5 V *vs.* Hg/Hg_2Cl_2. A pair of redox peaks from $[Fe(CN)_6]^{3+}$ is clearly evident. Strikingly, the peak current of the graphene/ZnO electrode is 25 times larger than that of glassy carbon electrode. In addition, the narrower potential separation between the anodic and cathodic peaks (ΔE_p) from the graphene/ZnO electrode as compared with that from the glassy carbon electrode (0.20 *vs.* 0.37 V) indicates that the graphene/ZnO electrode has a much higher charge transfer rate. The dependence of peak currents on scan rates (Fig. 6a inset) shows that the redox peak current increases linearly with the scan rate in the range from 5 mV s^{-1} to 100 mV s^{-1}, indicating a surface-controlled electrochemical process. Fig. 7b shows the amperometric current response of the graphene/ZnO electrode at the holding potential

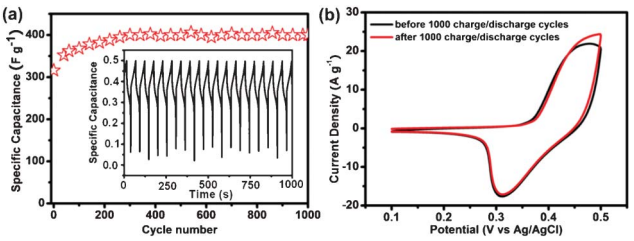

Fig. 6 (a) The cycle performance of graphene/ZnO hybrid electrode at the current density of 6.70 A g^{-1} in 2.0 M KOH solution. The inset shows the charge–discharge profile for the graphene/ZnO hybrid electrode. (b) CV of graphene/ZnO hybrid electrode before and after 1000 charge–discharge cycles.

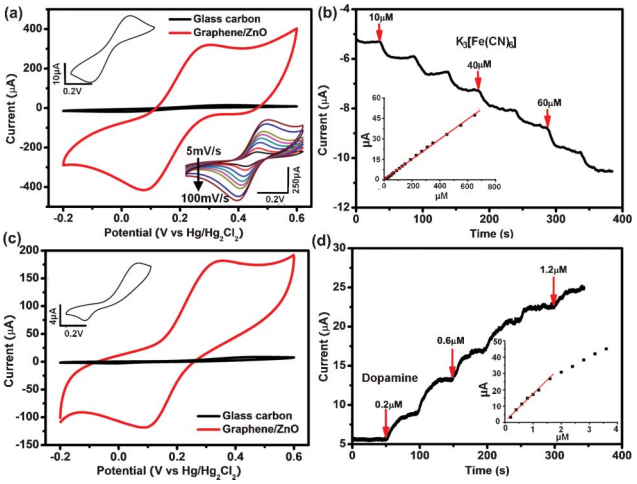

Fig. 7 (a) CV curves of a graphene/ZnO electrode and a glassy carbon electrode measured at the scan rate of 50 mV S^{-1} in 1.0 mM $K_3[Fe(CN)_6]$ PBS solution. The inset shows the enlarged CV curve of the glassy carbon electrode (left) and CV curves of the graphene/ZnO electrode in 1.0 mM $K_3[Fe(CN)_6]$ PBS solution at various scan rates of 5, 10, 20, 30, 40, 50, 80, 100 mV s^{-1} (right). (b) Amperometric response of the graphene/ZnO hybrid electrode upon addition of $K_3[Fe(CN)_6]$ into the PBS solution to various concentrations. Inset shows the relation between the magnitude of amperometric response and the concentration of $K_3[Fe(CN)_6]$. (c) CV curves of the graphene/ZnO and glassy carbon electrodes at the scan rate of 50 mV S^{-1} in 1.0 mM dopamine solution. The inset is the enlarged CV curve of glassy carbon electrode. (d) Amperometric response of the graphene/ZnO hybrid electrod upon addition of dopamine into PBS solution to various concentrations. Inset shows the current response *vs.* dopamine concentration.

of 0.1 V upon successive addition of $K_3[Fe(CN)_6]$ into PBS buffer solution. It is noted that the graphene/ZnO electrode gives a rapid and sensitive response. The dose response curve (magnitude of current decrease *vs.* ferricyanide concentration) is depicted in Fig. 7b (inset), which shows an extrapolated lower detection limit of ~10.0 nM (signal-to-noise ratio > 3), a sensitivity of 0.07 μA mM^{-1} cm^{-2}, and a wide linear detection range up to 800 μM.

Dopamine is a neurotransmitter and hormone, playing critical roles in central nervous, renal, endocrine, and cardiovascular systems.[48] The detection of dopamine is of great importance in biological studies, diagnosis, and drug screening. The detection of dopamine was attempted using the graphene/ZnO hybrid electrode. From its CV (Fig. 7c), a pair of redox peaks is observed. As compared with the glassy carbon electrode, it exhibits a narrower ΔE_p (0.25 *vs.* 0.5 V) suggesting a faster electron transfer rate and a much higher magnitude (~22 times) suggesting a higher sensitivity. The dose response curve (Fig. 7d inset) indicates an extrapolated lower detection limit of ~1.0 μM (signal-to-noise ratio > 3), a linear detection to 2.0 μM, and a sensitivity of 15.18 μA mM^{-1} cm^{-2}.

The high sensitivity and large detection range of the graphene/ZnO electrode can be attributed to its large specific surface area and high charge transfer rate. The latter is owing to the electroactive properties of ZnO nanorods and high conductive of 3D graphene foam. In addition, the porous structure of the electrode not only guarantees the large active surface area but

also ensures unhindered substance transport. These results demonstrate the promising potentials of 3D graphene/ZnO in the applications of electrochemical sensors.

3. Conclusions

Graphene/ZnO hybrid electrodes were fabricated by an *in situ* growth of ZnO nanorods on CVD grown graphene foams. Such free-standing, monolithic, 3D electrodes demonstrate excellent performance for supercapacitor and electrochemical detection, owing to its unique 3D architecture, electrochemical properties of ZnO, extraordinary electrical and mechanical properties of graphene, and the synergistic integration of the two types of nanomaterials. This study suggests that extending the 2D graphene into 3D architecture and hybridizing them with other functional nanomaterials would open new routes for the applications of graphene materials.

4. Experimental

4.1 Synthesis of 3D graphene and graphene/ZnO hybrid

3D graphene foams were synthesized by chemical vapor deposition (CVD) using nickel foam as the growth substrate[15] and ethanol as the carbon source under atmospheric pressure.[49,50] Nickel foams (1.0 mm thick, 2.0 × 2.0 cm) cleaned with acetone were loaded into a quartz tube and exposed to a 25 sccm H_2 and 50 sccm Ar environment while the temperature was raised to the growth temperature of 1000 °C. The quartz tube was held at this temperature for 10 min to clean the nickel surface. Ethanol vapor was then introduced into the quartz tube by bubbling H_2/Ar gas mixture through an ethanol liquid under ambient pressure. 20 min later, the ethanol vapor was cut off and the system was rapidly cooled to room temperature with a rate of ~100 °C min^{-1}. After growth, the nickel substrate was etched away with HCl (3 M) solution at 80 °C to obtain free-standing 3D graphene foams.

The graphene/ZnO hybrids were synthesized from $ZnCl_2$ in alkaline solution under hydrothermal condition.[51] In detail, 0.005 mol $ZnCl_2$ and 2.0 ml ammonia were dissolved into 40.0 ml deionized water and stirred thoroughly. Then, the mixture was transferred into a Teflon-lined stainless steel autoclave of 50 ml. The graphene foams fixing on glass slides were immersed into the solution and subjected to hydrothermal treatments at 120 °C for 1.5 h. After that, the autoclave was allowed to cool down to ambient temperature. Finally, the graphene/ZnO hybrids were obtained after washing and drying.

4.2 Characterizations of structure and morphology

The structures of graphene foams and graphene/ZnO hybrids were examined by Raman spectroscopy (laser wavelength 488 nm) (CRM200 Confocal Raman, WITec) and X-ray diffraction (XRD, Bruker D8 Advanced Diffrctometer using Cu Ka radiation). The morphology of the samples was revealed by field-emission scanning electron microscopy (JSM6700-FESEM, JEOL). Specific surface area was determined through measuring N_2 adsorption–desorption isotherm at 77 K using a Quantachrome NOVA-3000 system.

4.3 Electrochemical measurements

The electrochemical measurements were carried out in a three electrode electrochemical cell containing 2.0 M KOH as the electrolyte. The free-standing graphene/ZnO hybrid serves as the working electrode, an Ag/AgCl electrode as the reference, and a platinum wire as the counter electrode. Cyclic voltammetry (CV), galvanostatic charge–discharge and electrochemical impedance spectroscopy (EIS) were performed by a CHI660D electrochemical workstation (Chenhua, Shanghai) at room temperature. CVs were taken between 0.2 to 0.5 V at different scan rates. Galvanostatic charge–discharge curves were measured in the potential range of 0 to 0.5 V at different current densities. EIS measurements were carried out in the frequency range from 0.01 to 100 kHz at an open-circuit potential with a perturbation of 5.0 mV. The amperometric response measurements were carried out in phosphate buffered saline (PBS) solution (0.1 M, pH = 7.2).

Acknowledgements

We acknowledge the financial support from the NNSF of China (50902071, 61076067, BZ2010043), the National Basic Research Program of China (2009CB930601, 2012CB933300), Jiangsu Province Science Foundation for Six Great Talent Peak (RLD201103), A Project Funded by the Priority Academic Program Development of Jiangsu Higher Education Institutions, National Research Foundation of Singapore (CRP grant: NRF-CRP-07-2), Ministry of Education (AcRF tier 2 grant: MOE2011-T2-2-010).

References

1 K. S. Novoselov, A. K. Geim, S. V. Morozov, D. Jinag, Y. Zhang, S. V. Dubonos, I. V. Grigorieva and A. A. Firsov, *Science*, 2004, **306**, 666.
2 X. C. Dong, Y. M. Shi, Y. Zhao, D. M. Chen, J. Ye, Y. G. Yao, F. Gao, Z. H. Ni, T. Yu, Z. X. Shen, Y. X. Huang, P. Chen and L. J. Li, *Phys. Rev. Lett.*, 2009, **102**, 135501.
3 Y. Q. Sun, Q. Wu and G. Q. Shi, *Energy Environ. Sci.*, 2011, **4**, 1113.
4 J. B. Hou, Y. Y. Shao, M. W. Ellis, R. B. Moore and A. L. Yi, *Phys. Chem. Chem. Phys.*, 2011, **13**, 15384.
5 Y. X. Liu, X. C. Dong and P. Chen, *Chem. Soc. Rev.*, 2012, **41**, 2283.
6 Y. X. Huang, X. C. Dong, Y. M. Shi, C. M. Li, L. J. Li and P. Chen, *Nanoscale*, 2010, **2**, 1485.
7 Y. X. Huang, X. C. Dong, Y. X. Liu, L. J. Li and P. Chen, *J. Mater. Chem.*, 2011, **21**, 12358.
8 S. J. He, B. Song, D. Li, C. F. Zhu, W. P. Qi, Y. Q. Wen, L. H. Wang, S. P. Song, H. P. Fang and C. H. Fan, *Adv. Funct. Mater.*, 2010, **20**, 453.
9 L. H. Wang, K. Y. Pu, J. Li, X. Y. Qi, H. Li, H. Zhang, C. H. Fan and B. Liu, *Adv. Mater.*, 2011, **23**, 4386.
10 Y. W. Zhu, S. Murli, W. W. Cai, X. S. Li, J. W. Suk, J. R. Potts and R. S. Ruoff, *Adv. Mater.*, 2010, **22**, 3906.
11 V. Singh, D. Joung, L. Zhai, D. Soumen, K. Saiful and S. Sudipta, *Prog. Mater. Sci.*, 2011, **56**, 1178.
12 O. C. Compton and S. T. Nguyen, *Small*, 2010, **6**, 711.
13 E. Goki and C. Manish, *Adv. Mater.*, 2010, **22**, 2392.
14 X. C. Dong, C. Y. Su, W. J. Zhang, J. W. Zhao, Q. D. Ling, W. Huang, P. Chen and L. J. Li, *Phys. Chem. Chem. Phys.*, 2010, **12**, 2164.
15 Z. P. Chen, W. C. Ren, L. B. Gao, B. L. Liu, S. F. Pei and H. M. Cheng, *Nat. Mater.*, 2011, **10**, 424.
16 X. Huang, X. Y. Qi, F. Boey and H. Zhang, *Chem. Soc. Rev.*, 2012, **41**, 666.
17 D. Q. Liu, Q. Wang, L. Qiao, F. Li, D. S. Wang, Z. B. Yang and D. Y. He, *J. Mater. Chem.*, 2012, **22**, 483.
18 S. K. Meher and G. R. Rao, *J. Phys. Chem. C*, 2011, **115**, 15646.
19 Z. L. Wang, R. Guo, G. R. Li, L. X. Ding, Y. N. Qu and Y. X. Tong, *RSC Adv.*, 2011, **1**, 48.
20 J. T. Li, W. Zhao, F. Q Huang, A. Manivannan and N. Q. Wu, *Nanoscale*, 2011, **3**, 5103.

21 R. L. Liang, H. Q. Cao and D. Qian, *Chem. Commun.*, 2011, **47**, 10305.
22 Z. J. Fan, J. Yan, T. Wei, L. J. Zhi, G. Q. Ning, T. Y. Li and F. Wei, *Adv. Funct. Mater.*, 2011, **21**, 2366.
23 Q. Cheng, J. Tang, J. Ma, H. Zhang, N. Shinya and L. C. Qin, *Carbon*, 2011, **49**, 2917.
24 P. L. Brize and M. Arben, *Adv. Funct. Mater.*, 2011, **21**, 255.
25 C. W. Kung, C. Y. Lin, Y. H. Lai, R. Vittal and K. C. Ho, *Biosens. Bioelectron.*, 2011, **27**, 125.
26 G. Irene and L. Monica, *Energy Environ. Sci.*, 2009, **2**, 19.
27 J. S. Wu and D. F. Xue, *Sci. Adv. Mater.*, 2011, **3**, 127.
28 X. B. Hu, H. J. Zhang, Y. W. Ni, Q. Zhang and J. P. Chen, *Biosens. Bioelectron.*, 2008, **24**, 93.
29 X. C. Dong, Y. M. Shi, P. Chen, Q. D. Ling and W. Huang, *J. J. Appl. Phys.*, 2010, **49**, 01AH04.
30 A. Reina, X. T. Jia, J. Ho, D. Nezich, H. Son, V. Bulovic, M. S. Dresselhaus and J. Kong, *Nano Lett.*, 2009, **9**, 30.
31 D. Graf, F. Molitor, K. Ensslin, C. Stampfer, A. Jungen, C. Hierold and L. Wirtz, *Nano Lett.*, 2007, **7**, 238.
32 J. F. Scott, *Phys. Rev. B*, 1970, **2**, 1209.
33 A. C. Ferrari and J. Robertson, *Phys. Rev. B*, 2000, **61**, 14095.
34 X. C. Dong, D. L. Fu, W. J. Fang, Y. M. Shi, P. Chen and L. J. Li, *Small*, 2009, **5**, 1422.
35 S. Park, J. An, J. R. Potts, A. Velamakanni, S. Murali and R. S. Ruoff, *Carbon*, 2011, **49**, 3019.
36 J. Wang, Z. Gao, Z. S. Li, B. Wang, Y. T. Yan, Q. Liu, T. Mann, M. L. Zhang and Z. H. Jiang, *J. Solid State Chem.*, 2011, **184**, 1421.
37 Y. P. Zhang, H. B. Li, L. K. Pan, T. Lu and Z. Sun, *J. Electroanal. Chem.*, 2009, **634**, 68.
38 Y. L. Chen, Z. A. Hu, Y. Q. Chang, H. W. Wang, Z. Y. Zhang, Y. Y. Yang and H. Y. Wu, *J. Phys. Chem. C*, 2011, **115**, 2563.
39 X. H. Xia, J. P. Tu, X. L. Wang, D. C. Gu and X. B. Zhao, *Chem. Commun.*, 2011, **47**, 5786.
40 X. Y. Peng, X. X. Liu, D. Diamond and K. T. Lau, *Carbon*, 2011, **49**, 3488.
41 Q. Wu, Y. X. Xu, Z. Y. Yao, A. R. Liu and G. Q. Shi, *ACS Nano*, 2010, **4**, 1963.
42 J. Wang, Z. Gao, Z. Li, B. Wang, Y. Yan, Q. Liu, T. Mann, M. Zhang and Z. Jiang, *J. Solid State Chem.*, 2011, **184**, 1421.
43 T. Lu, L. Pan, H. Li, G. Zhu, T. Lv, X. Liu, Z. Sun, T. Chen and D. H. Chua, *J. Alloys Compd.*, 2011, **509**, 5488.
44 J. Zhang, L. B. Kong, J. J. Cai, Y. C. Luo and L. Kang, *J. Solid State Electrochem.*, 2010, **14**, 2065.
45 E. Frackowiak and F. Begguin, *Carbon*, 2001, **39**, 937.
46 W. H. Shi, J. X. Zhu, D. H. Sim, Y. Y. Tay, Z. Y. Lu, X. J. Zhang, Y. Sharma, M. Srinivasan, H. Zhang, H. H. Hng and Q. Y. Yan, *J. Mater. Chem.*, 2011, **21**, 3422.
47 J. Zhang, L. Wang, D. Pan, S. Song and C. H. Fan, *Chem. Commun.*, 2007, 1154.
48 J. Weng, J. Xue, J. Wang, J. Ye, H. Cui, F. Sheu and Q. Zhang, *Adv. Funct. Mater.*, 2005, **15**, 639.
49 X. C. Dong, B. Li, A. Wei, X. H. Cao, M. B. Chan-Park, H. Zhang, L. J. Li, W. Huang and P. Chen, *Carbon*, 2011, **49**, 2944.
50 X. C. Dong, P. Wang, W. Fang, C. Y. Su, Y. H. Chen, L. J. Li, W. Huang and P. Chen, *Carbon*, 2011, **49**, 3672.
51 A. Wei, Z. Wang, L. H. Pan, W. W. Li, L. L. Xiong, X. C. Dong and W. Huang, *Chin. Phys. Lett.*, 2011, **28**, 080702.